



HAL
open science

Photochemical Imaging of Near-Field and Dissymmetry Factor in Chiral Nanostructures

Thinhinane Aoudjit, Andreas Horrer, Sergei Kostcheev, Renaud Bachelot, Jérôme Plain, Davy Gérard

► **To cite this version:**

Thinhinane Aoudjit, Andreas Horrer, Sergei Kostcheev, Renaud Bachelot, Jérôme Plain, et al.. Photochemical Imaging of Near-Field and Dissymmetry Factor in Chiral Nanostructures. *Advanced Optical Materials*, 2023, 11 (9), pp.2203015. 10.1002/adom.202203015 . hal-04097334

HAL Id: hal-04097334

<https://utt.hal.science/hal-04097334>

Submitted on 15 May 2023

HAL is a multi-disciplinary open access archive for the deposit and dissemination of scientific research documents, whether they are published or not. The documents may come from teaching and research institutions in France or abroad, or from public or private research centers.

L'archive ouverte pluridisciplinaire **HAL**, est destinée au dépôt et à la diffusion de documents scientifiques de niveau recherche, publiés ou non, émanant des établissements d'enseignement et de recherche français ou étrangers, des laboratoires publics ou privés.



Distributed under a Creative Commons Attribution 4.0 International License

Photochemical imaging of near-field and dissymmetry factor in chiral nanostructures

Thinhinane Aoudjit, Andreas Horrer, Sergei Kostcheev, Renaud Bachelot,

Jérôme Plain,* and Davy Gérard*

Light, nanomaterials, nanotechnologies (L2n), Université de Technologie de Troyes, CNRS

EMR 7004, 12 rue Marie Curie, Troyes 10004, France

E-mail: jerome.plain@utt.fr; davy.gerard@utt.fr

Abstract

Chiral nanostructures interact differently with right- or left-handed circularly polarized light. Due to the lack of experimental approaches able to unveil the optical near-field around chiral nanostructures, their optical characterization generally relies either on far-field techniques or on numerical simulations. Here, a subwavelength imaging approach based on the interaction between the enhanced optical near-field around chiral nanoparticles and an azobenzene molecular probe is reported. Under the action of light, the azobenzene molecules undergo isomerization cycles resulting in a measurable displacement of matter. The resulting imprint of the optical near-field can then be imaged using atomic force microscopy. Using two shifted gold nanorods separated by a nanogap as a canonical chiral structure, a dissymmetry in the near-field of the chiral structures under left and right circular polarizations is experimentally evidenced. Notably, it is observed that the gap mode is excited only when the handedness of the exciting light matches the handedness of the nanostructure, evidencing a chiral hot spot inside the gap. Moreover, it is shown that it is possible to experimentally map the near-field dissymmetry factor, a quantity related to the local circular dichroism of the near-field intensity.

Introduction

Chiral nanostructures have recently attracted a lot of attention. An object or group of objects is said to be chiral if it cannot be superimposed to its mirror image.¹ These two mirror images (called enantiomers for molecules) interact differently with circularly polarized light, giving birth to *chiroptical effects*, which include optical rotation, circular dichroism and vibrational optical activity, to name a few.² Chirality is ubiquitous in nature and can be observed at various scales, however the magnitude of chiroptical interactions is generally weak. For instance, the circular dichroism spectrum of most biomolecules peaks in the ultraviolet range.³ In contrast, chiral nanostructures can yield large chiroptical interactions near

their resonance frequency, which can be tuned by changing the opto-geometrical parameters of the structure. In this context, different planar (2D) and 3D chiral nanostructures have been developed to enhance chiroptical effects using different configurations and geometries (see e.g., Ref.^{2,4,5} for reviews). For instance, chiral nanostructures and metasurfaces were used to polarize light,^{6,7} to enhance the emission of circularly polarized light⁸ and to enhance second harmonic generation.⁹

All of the aforementioned effects were observed in far-field. However, it is well-known that resonant nanostructures generate a very strong response in their near-field. Chiral nanostructures also exhibit a strong near-field response, provided that they are excited by light with the same handedness as the structure.¹⁰ In particular, Tang and Cohen demonstrated that the excitation rate of a chiral molecule under right-handed (RCP) or left-handed (LCP) circular polarization is directly related to the local value of a quantity called the optical chirality C .¹¹ In a nutshell, the optical chirality quantifies how the electromagnetic field is locally twisted. In the case of plane waves it is bounded to a maximum value obtained for circularly polarized waves, but in the near-field of a chiral nanostructure it can be locally enhanced beyond this limit, reaching values far above its bounded far-field value – a phenomenon called super-chirality. This is why chiral nanostructures are extremely interesting for the enantio-selective detection of chiral molecules,^{12,13} to increase the enantiopurity of photochemical reactions,¹⁴ and to selectively enhance photocatalysis.¹⁵ Albeit easy to compute with an electromagnetic solver, optical chirality has remained elusive experimentally – as it would require the simultaneous measurement of both the electric and magnetic fields. In order to quantify the polarization-dependent behavior of the electromagnetic field around chiral nanostructures, an alternative quantity has been recently proposed: the *near-field dissymmetry factor*.^{16,17} Chiral objects present a different spatial distribution of their optical near-field depending on the direction of the circular exciting polarization, LCP or RCP. This can be quantified by computing the contrast in the local near-field response of the object

under RCP and LCP excitations:

$$V(\vec{r}) = \frac{|E_{\text{LCP}}(\vec{r})|^2 - |E_{\text{RCP}}(\vec{r})|^2}{|E_{\text{LCP}}(\vec{r})|^2 + |E_{\text{RCP}}(\vec{r})|^2} \quad (1)$$

where $E_{\text{LCP}}(\vec{r})$ and $E_{\text{RCP}}(\vec{r})$ are the electric field amplitudes at position \vec{r} under LCP and RCP excitations, respectively. Hence, $V(\vec{r})$ quantifies the local near-field dissymmetry (or imbalance) between the RCP and LCP polarizations around the nanostructure. It can also be understood as the local circular dichroism of the near-field intensity.

In order to understand the origin of chirality and to directly image the near-field behaviour of chiral nanostructures under left- or right-handed circular polarization, different imaging techniques have emerged. Examples include near-field optical microscopy,^{18,19} second-harmonic generation (SHG) microscopy,²⁰ cathodoluminescence¹⁶ and photon-induced near-field electron microscopy.²¹ In this paper, we use a photochemical imaging method based on the interaction of the local field around the nanostructure with a photosensitive polymer.²² The polymer consists of azobenzene molecules (Disperse Red One, DR1) grafted to a polymethylmetacrylate (PMMA) backbone (Figure S1a). DR1 has two different spatial configurations: the *trans* and *cis* diastereoisomers. Under excitation at a suitable wavelength, DR1 molecules absorb light and, via a process known as photo-isomerization, transform this electromagnetic energy into a configurational change from the *trans* to the *cis* state. The isomerization cycles induce molecular displacement and migration of matter from high electric field intensity to low intensity areas. This light-induced displacement of matter leads to topographic changes in the surface of PMMA-DR1 that can be subsequently observed with an atomic force microscope (AFM). The resulting AFM images can be seen as nanoscale "snapshots" of the local optical intensity. This photochemical imaging technique was successfully applied to the imaging of surface plasmon resonances in metallic nanoparticles^{23,24} and gap antennas.²⁵ Strictly speaking, the PMMA-DR1 is sensitive to both the in-plane and out-of-plane components of the exciting electromagnetic field. It has been demonstrated

that out-of-plane components leads to matter accumulation in high electric field intensity zones, whereas in-plane near-field components leads to matter depletion.^{23,26} Recently, we used this technique on achiral plasmonic metamolecules and experimentally evidenced chiral near-field distributions.¹⁷ In the following, we study the near-field response and the visibility factor of chiral metallic nanostructures by photochemical imaging. The nanostructures are two coupled gold nanorods that are shifted with respect to each other along their long axis. This geometry, inspired from the coupled nanorods studied in Ref.²⁷ allows one to tune the geometrical chirality of the structure by changing the value of the shift. The experimental results from the photochemical imaging are compared with numerical simulations. We experimentally obtain photochemical images of the dissymmetric electric field intensity around the chiral nanostructures. Moreover, we show that the depth of the polymer depletion inside the gap is correlated to the value of the field intensity. Finally, we show that it is possible to experimentally image the near-field dissymmetry factor $V(\vec{r})$ by subtracting the photochemical images obtained under both circular polarizations.

Experimental approach

The structure, shown in Figure 1a, is composed of two coupled gold nanorods. Each rod has a length of 140 nm, a width of 70 nm and a height of 50 nm. They are separated by a 40 nm wide gap and are shifted with respect to each other by a distance s along their long axis (y -direction). Coupled nanorods – as well as their complementary structure, coupled nanoslits²⁸ – can be seen as the canonical planar chiral geometry, notably because it is possible to tune the degree of structural chirality of the structure simply by shifting one rod with respect to the other.^{27,29} This structural (or geometrical) chirality can be quantified using a simple metric inspired from the chiral coefficient χ coined by Gilat.³⁰ For a planar structure it can be easily computed as $\chi_{2D} = S_{\text{NO}}/S_0$, where S_0 is the total projected surface of the structure and S_{NO} the non-overlapping projected surface between the structure and its mirror image

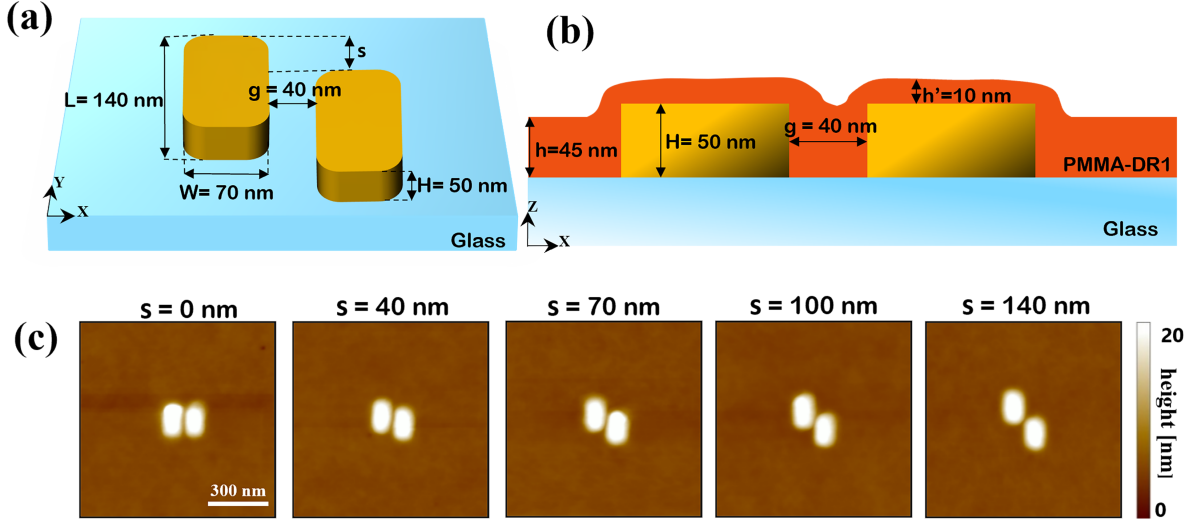


Figure 1: (a) Schematic of the investigated plasmonic nanostructures before polymer deposition. s is the value of rod shift in the y direction. (b) Schematic side-view of the structures after PMMA-DR1 deposition. The indicated thicknesses are experimental values obtained by comparing AFM images taken before and after deposition. (c) $1\mu\text{m} \times 1\mu\text{m}$ AFM images of the five different structures after deposition of the 45-nm thick layer of PMMA-DR1.

(see Figure S2). For an achiral structure, the mirror images perfectly overlap and $\chi_{2D} = 0$, while for totally non-overlapping structures $\chi_{2D} = 1$. It is clear from Figures 1 and S2 that the value of χ_{2D} can be continuously tuned from 0 to 1 simply by shifting the nanorods.

We designed five different structures where s was varied from 0 to 140 nm. Thus, for $s = 0$ the two nanorods form an achiral structure and the chiral aspect of the structure increases when increasing s . The values of χ_{2D} for the studied structures are shown in Figure S2. The size of the nanorods was chosen in order to obtain structures resonating around $\lambda = 900$ nm, a wavelength lying within the 2-photon absorption band of PMMA-DR1.^{17,25} The resonance wavelength was computed using the Finite Difference Time Domain (FDTD) method (see Methods for details). The FDTD-computed absorption spectra for different values of the relative shift between the nanorods s is shown in the Supplementary information (Figure S3). Although the extinction spectrum is slightly modified (red-shifted) when s increases, the excitation wavelength $\lambda = 900$ nm (vertical line in Figure S3) remains close to the extinction peak.

The nanostructures were fabricated by electron beam lithography on a glass substrate and then covered with a 45-nm thick layer of PMMA-DR1 (see Methods and Figure 1b). Figure 1c presents AFM images of the structures after deposition of the PMMA-DR1. This thickness was chosen because thin layers are more sensitive to the near-field, while thicker layers are sensitive to both near-field and the far-field in the Fresnel zone.²⁴ Then, the system composed of the nanostructure and the PMMA-DR1 film is irradiated by the beam from a pulsed Ti:Sa laser, whose emitting wavelength is $\lambda = 900$ nm lies in the absorption spectrum of the PMMA-DR1 co-polymer (see red curve in Figure S1b). The power density and exposure time were 500 mW/m^2 and 30 s, respectively.

Results and discussion

Photochemical imaging

First, we report on the photochemical imaging of the chiral structures. AFM images measured on the photopolymer-covered structures after interaction with circularly-polarized light are shown in Figure 2(a,c) (see Methods for details on AFM imaging). The experimental images are compared to the FDTD calculation of the total electric field intensity under LCP (Figure 2b) and RCP (Figure 2d) polarizations. Note that strictly speaking, 2-photon absorption being a second-order non linear process, its strength is governed by the square of the electric field intensity $|E|^4$. However, in accordance with our previous work,¹⁷ we observed that the maps of the spatial distribution of $|E|^4$ and $|E|^2$ are very similar, only their magnitude changes (Figure S4a). Hence, in the following, the experimental images are compared with the electric field intensity.

Similarly to other non linear effects, two-photon absorption presents a threshold effect, filtering out weaker exciting intensities. In other words, absorption occurs only if the local field intensity reaches a threshold value. The analysis of the AFM images reveals a displacement of material in the plane of the sample induced essentially by the E_x and E_y components

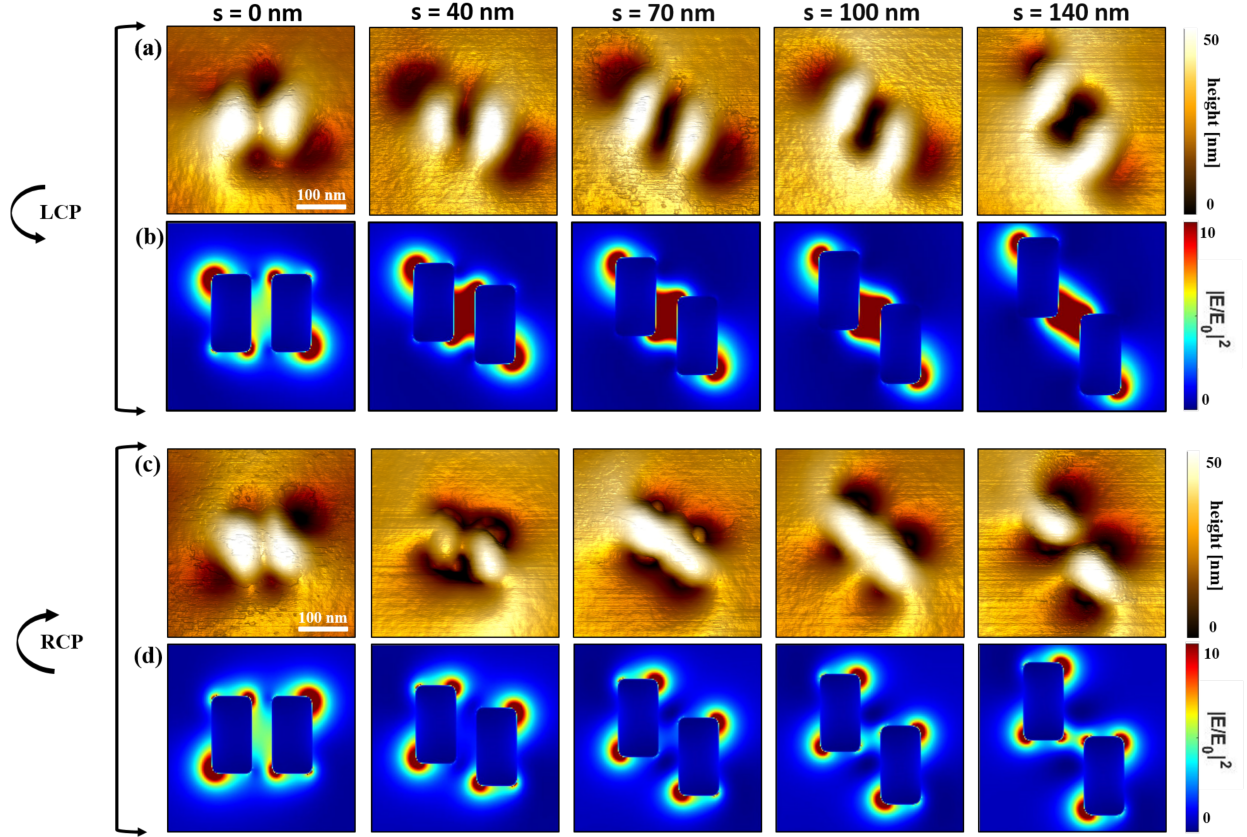


Figure 2: (a,c) AFM images of the different nanostructures after a 30 s irradiation using left-handed (LCP) and right-handed (RCP) circularly polarized light at $\lambda = 900$ nm. (b,d) FDTD-calculated total electric field intensity for the different nanostructures under LCP and RCP excitations.

of the field (see Figure S4b). The intensity of the (weak) E_z component of the field is filtered out, hence the absence of an accumulation or an elevation of matter around the structures.

The photopolymer-covered structures were first illuminated using LCP light. The corresponding AFM images showing the polymer surface after illumination are shown in Figure 2a. The AFM images show the appearance of dark zones around the structures, which correspond to areas where matter depletion is observed. Comparing the experimental results to FDTD calculations of total electric field intensity (Figure 2b) shows that the depletion areas are nicely correlated to regions where the near-field intensity is high. In particular, a clear depletion is observed in the gap between the nanorods, indicating the excitation of a gap mode. The intensity in the gap is stronger for chiral structures (i.e. $\chi_{2D} \neq 0$). Moreover,

the higher is the relative shift between the nanorods (and hence the structural chirality), the more dissymmetric is the near-field distribution around the structures. Interestingly, even for the achiral structure, a dissymmetric field distribution is observed. This effect has already been observed experimentally¹⁹ and can be explained by the interference between spectrally-overlapping eigenmodes in the structure.^{17,31} The link between field dissymmetry and structural chirality will be explored in more depth using the V -factor later on.

Then, the polymer-covered structure was rinsed with toluene to completely dissolve the PMMA-DR1 layer and a new layer was spin-coated. Finally, the sample was illuminated using the same dose under RCP excitation, and AFM imaging was performed at the same exact location (Figure 2d). Hence, the experimental AFM images for both polarizations can be directly compared. Here also, we note that the location of the depletion zones corresponds to the theoretically calculated high intensity zones. A striking feature is the absence of light intensity enhancement inside the gap for chiral structures under RCP excitation. Hence, the gap mode in the chiral nanorods acts as a handedness-dependent "hot spot". Moreover, this allows us to characterize the handedness of the structures: as the gap lights up only under LCP excitation, the structures are left-handed.

Local field intensity

The above results demonstrate that photochemical imaging allows us to qualitatively image the near-field spatial distribution around the structure. Now, we would like ask the following question: can we obtain from the AFM image a more quantitative information about the field intensity? To address this question, we focus on the photopolymer response inside the gap. Figure 3(a-e) shows linecuts through the photopolymer-covered structures, before (black lines) and after (colored lines) a 30 s irradiation with LCP light. In Figure 3f, we plot the different values of the depth of the holes induced by matter migration inside the gap (red dots, the line is a guide for the eye) and compare these values to the computed squared field intensity I^2 at the center of the gap (light blue dots).

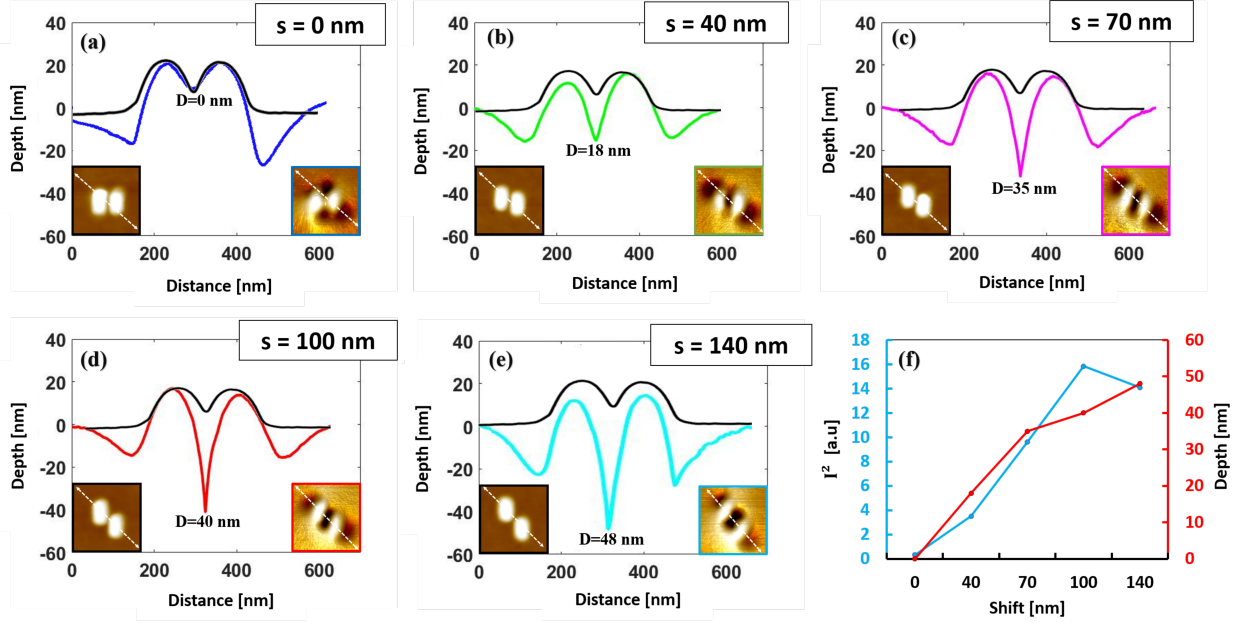


Figure 3: (a-e) AFM profiles obtained before (black lines) and after (colored lines) irradiation with LCP light of the different structures. D is the depth of the hole formed by the migration of matter in the gap, after a 30 s irradiation with a Ti:Sa laser emitting 500 mW/cm^2 at $\lambda = 900 \text{ nm}$. Insets are $500 \text{ nm} \times 500 \text{ nm}$ AFM images recorded before (left panel) and after (right panel) illumination. (f) Comparison of the hole depth (red dots) and the square of the electric field intensity I^2 in the gap for different values of s . I^2 was computed using FDTD and evaluated at the geometrical center of the gap.

We first notice that the hole depth continuously increases as a function of the value of s . The formed hole is deeper for high values of the structural chirality. In contrast, we also notice that the field intensity in the gap of the nanostructure first increases with s , and decreases slightly for $s > 140 \text{ nm}$. This is mainly due to the contribution of the electromagnetic coupling between the two nanorods, which increases with increasing values of s , reaching a maximum for $s = 100 \text{ nm}$. However, for higher values of s , the coupling starts to decrease as the nanorods are located further apart from each other. This results in a lower value of I^2 at $s = 140 \text{ nm}$ than at $s = 100 \text{ nm}$. On the other hand, the AFM profiles from photochemical imaging reveal a greater depth for $s = 140 \text{ nm}$. This can be explained by considering that matter migration is driven not only by the local electromagnetic intensity, but also by the availability of free space into which PMMA-DR1 molecules can move. As the $s = 140 \text{ nm}$ structure exhibits larger open surfaces in its gap, this facilitates molecular displacement,

largely compensating the decrease of the local intensity. An interesting conclusion is that in the case of the coupled nanorods, the photochemical imaging technique directly probes the structural chirality *via* the matter depletion in the gap (the deeper the hole formed in the gap, the stronger the structural chirality).

To further explore the role of field intensity on the photo-induced matter displacement, we compare in Fig. S5 the computed field intensity for two chiral structures (Fig. S5a) to the experimental AFM maps (Fig. S5b). To obtain the value of the light-induced matter displacement, we made a subtraction between the AFM image taken before illumination and the image taken after illumination with LCP light (see the inset of Fig. S5b). The comparison is made along a line-cut across the gap and parallel to the long axis of the nanorods (white dashed lines in Fig. S5). In Fig. S5a, one can see that the computed field intensities for the $s = 40$ nm and $s = 70$ nm structures have very similar profiles, with a strong difference (about 3 times) in their maximum field intensities. In contrast, the experimental maps from Fig. S5b exhibit a much smaller difference in the measured depths (from ~ 25 nm for $s = 40$ nm to ~ 35 nm for $s = 70$ nm), although following qualitatively the same trend. Again, this is due to the fact that the photo-induced matter displacement depends not only on the local field intensity, but also on matter availability where the field is (molecules to be moved) and also on free space availability nearby (space for the molecules to move in).

Summarizing our results, we can now say that the photochemical maps taken on structures with different geometries can only be qualitatively compared with the local electric field intensity. However, a more quantitative comparison can be made when comparing images taken from the same structure, as we show in the next section.

Near-field dissymmetry factor

As explained in the introduction, the near-field dissymmetry factor V is the optical contrast between the local near-field intensities under LCP and RCP excitation. Since our photochemical approach yields maps where the polymer height after illumination is related to the

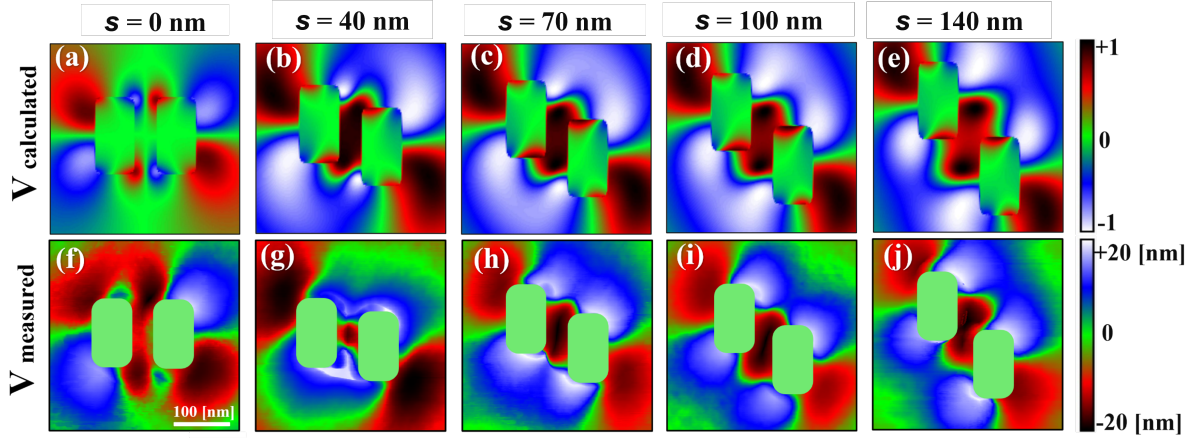


Figure 4: Imaging of the near-field dissymmetry factor V . (a-e) Theoretical maps of the V -factor calculated from the simulation results of the total electric field. (f-j) Experimental maps of the V -factor obtained from the subtraction of the AFM images from the two polarizations.

local near-field intensity, one may wonder if it is possible to experimentally map the V -factor. The FDTD-computed V -factor for five structures with different structural chiralities is shown in Figure 4a-e. In these maps, the red-colored zones correspond to regions with $V > 0$, these are areas where the electromagnetic field intensity is mostly LCP, whereas blue-colored zones correspond to the regions where it is mostly RCP. *Locally* the electromagnetic field can be left- or right-handed. For the achiral structure (Figure 4a), the blue- and red-colored zones exhibit identical areas (the map is symmetrical), but when the structural chirality increases, there is an imbalance between the blue- and red-colored areas. To quantitatively evaluate the evolution of the V -factor, we plotted in Figure S6a the value of V (taken at the center of the gap and calculated at $\lambda = 900$ nm) as a function of the structural chirality. Starting from $V = 0$ at $s = 0$, the V -factor quickly increases with s , and thus with the structural chirality χ_{2D} , reaching a maximum for $s = 40$ nm and $s = 70$ nm. It should be noted that the value of V depends on the wavelength (Figure S5a), and if V is measured at its peak value rather than at a fixed wavelength, the maximum field dissymmetry is obtained around $s = 70$ nm (Figure S6b, blue curve). This value corresponds to a situation where the rods are shifted by a distance corresponding to half their length –

a configuration reported to lead to the highest optical chirality.²⁸

We directly subtracted the two AFM images obtained under LCP (Figure 2a) and RCP (Figure 2c) illumination, respectively, to obtain an experimental contrast map. We underline that such a direct subtraction is possible because the experimental images were obtained on the very same structures using the same illumination conditions (only the polarization state of the exciting light changes). The result of this procedure is shown in Figure 4f-j, using the same color-coding (red corresponds to areas where the LCP AFM map is deeper than the RCP one, i.e. it is left-handed). Note that for the sake of clarity, in the experimental images the areas corresponding to the position of the nanorods have been excluded from the subtraction and appear in green. A remarkable agreement is found between these experimental maps and the theoretical maps of the V -factor. However, one can notice that for the achiral structure, photochemical imaging hardly resolves all four lobes within the gap (compare Figure 4a and f). This can be explained by taking into account that the nanorods themselves can hinder the movement of molecules, limiting the spatial resolution in confined areas such as nanogaps. Note that in principle, it should be possible to normalize the experimental maps of V , simply by dividing the images in Figure 4f-j by the sum of the AFM images for LCP and RCP. However, we observed that this procedure introduced too much noise in the experimental maps without adding any useful physical information.

This result demonstrates the capability of photochemical imaging to quantify the near-field dissymmetry, a quantity which is related to the structural chirality of the considered structure. A closer look at the near-field dissymmetry maps of Figure 2 reveals an interesting result about the chiral nanorods. Inside the gap, the chirality of the near-field distribution (as quantified by the V -factor) is globally left-handed. In contrast, outside the gap the maps are dominated by blue-colored areas, indicating a globally right-handed chirality. The optical near-fields for the inner and outer surroundings of the chiral nanorods hence appears to have opposite handedness.

Finally, it is also interesting to compare the V -factor to other metrics of the chirality,

such as the optical chirality C and the circular dichroism CD . These quantities are plotted in Fig. S6c and e, respectively, as a function of the exciting wavelength. A comparison with the V -factor (computed at the center of the gap) is also provided in Fig. S6d,f. First, one can observe that the normalized optical chirality (Fig. S6c) and CD (Fig. S6e) show a similar behavior with respect to the geometrical chirality, as they are both maximum for the $s = 100$ nm structure. In contrast, the near-field dissymmetry is not maximum for this structure, but at smaller shifts. This is due to the fact that the V -factor depends only on the electric field intensity. For $s = 100$ nm, the polarization-independent high electric field excited at the structure's corners reaches the center of the gap (where V and C are computed). The optical chirality is less sensitive to this effect as it also depends on the value of the magnetic field.

Conclusion

To conclude, we studied the near-field response of chiral planar plasmonic nanostructures. The structural chirality was continuously tuned from an achiral structure to a very chiral structure by shifting one nanorod with respect to the other. Using a photochemical imaging technique, we directly observed the spatial distribution of the optical intensity around the structure. In particular, we experimentally evidenced a light spin-dependent excitation of the gap mode in the coupled nanorods, as light is observed in the gap only when the handedness of the exciting light matches the handedness of the nanostructure. Such chiral hot spots could be used to tailor the emission of quantum emitters located in the gap, leading to chiral light emission.^{32,33}

Furthermore, the dissymmetry in the optical near-field generated by the structures was obtained, simply by subtracting the experimental images obtained under LCP and RCP excitation. We showed that the chirality of the electromagnetic response of structures, as quantified by the V -factor, depends on their structural chirality. In particular, the contrast

between the near-field response under left-handed and right-handed polarization increases with the geometrical chirality of the nanostructures. The experimental results were further confirmed by the numerical simulations taking into account the experimental conditions. We emphasize that the technique can be applied to any planar chiral structure. Although the displacement of the molecular probe can be hindered in nanogaps, it should be underlined that the near-field dissymmetry can be imaged inside a 40 nm wide gap, evidencing the nanoscale resolution of the approach.

Experimental Section

FDTD calculations

The FDTD simulations were performed using a commercial software (Ansys Lumerical). The computation box was a $2 \times 2 \times 2 \mu\text{m}^3$ cube with PLM boundary conditions on all faces. The computation time was set to 10000 fs. A constant mesh size of 2 nm was chosen to model the nanostructure area. The structures were illuminated under normal incidence from the substrate side. To model left-handed (LCP) and right-handed (RCP) circular polarizations, two TFSF (Total Field Scattered Field) sources were used, phase-shifted by $\pm 90^\circ$.

The refractive index of the substrate was set to $n = 1.5$. Above the substrate an effective refractive index of $n = 1.7$ was chosen to model the PMMA-DR1 layer. The total near-field intensity was evaluated in a plane crossing through the structures and located 40 nm above the substrate surface.

Sample fabrication

The structures were fabricated using electron-beam lithography (EBL) and lift-off process. Starting from a clean glass substrate (microscope coverslip), we spin-coated a 160-nm-thick layer of polymethylmetacrylate (PMMA) dissolved in methylsobutylketone (MIBK) at a concentration of 30 g/L on the substrate. Knowing that the ratio between the thickness of

the PMMA and the estimated height of the nanostructures is 1/3, this thickness will allow us to deposit 50 nm of gold. The polymer was then annealed for 3h at 160° to obtain a homogeneous surface and to evaporate solvent residues. For the EBL step, a conductive polymer layer was deposited. It will be removed directly after etching by rinsing the sample with deionized water. The nanofabrication of the structures was performed by an electron beam using a scanning electron microscope. The different exposure parameters allow us to control the dimensions of the structures. In our case, we used an aperture of 10 mm giving a beam of 20 nm diameter accelerated to 20 kV with a current of 8 pA. The deposited dose was 380 $\mu\text{C}/\text{cm}^2$.

In order to reveal the shape of the structures, we immersed our sample in a MIBK / Isopropanol solution for one minute and then in pure isopropanol for 15 s in order to dissolve the exposed resin. Then, the deposition of the gold layer was done by Joule-effect evaporation of the metal under a pressure of about 10^{-7} mBar and with a deposition rate of about 0.2 nm/s. A 3-nm thick layer of titanium dioxide (TiO_2) was deposited beforehand to ensure the adhesion of the gold to the substrate. Finally, the metal layer deposited on the unexposed resist was lifted-off by placing the sample in acetone for a minimum of 3 hours.

Photochemical imaging

The azobenzene molecule used in this work is Disperse Red1, or 4-(N-(2-hydroxyethyl)-N-ethyl)amino-4'-nitriazobenzene. This molecule is grafted to a PMMA polymer with a molar ratio of 30%. First, the PMMA-DR1 powder was dissolved in a solution of methyl butyl ketone (MIBK), known to be the most suitable solvent for PMMA. The concentration of the solution used was 20 g/L. The solution was stirred for a minimum of 1 h to ensure that the copolymer was soluble in the solvent. Then, the solution was purified using a syringe and a filter. Finally, the PMMA-DR1 was spin-coated using a speed of 3000 rpm and an acceleration of 4000 rpm/s. This procedure yields a 45-nm polymer layer thickness above the substrate, as measured by atomic force microscopy (AFM). However, the polymer is

only 10-nm thick above the gold structures (as the deposition is not a conformal coating, see Figure 1b).

To irradiate the sample, we used a Ti:Sa laser emitting at $\lambda = 900$ nm. The laser being linearly polarized, the polarization of the beam was turned into the left-handed (LCP) or the right-handed (RCP) polarization using a quarter-wave plate (AQWP05M-980 from Thorlabs). The polarization state was further checked using a polarimeter. The laser was focused onto the surface of the sample using an objective lens with x10 magnification and 0.3 numerical aperture. We used a laser power fixed at $1 \mu\text{W}$. The diameter of the laser spot on the sample being $4 \mu\text{m}$, this yields a power density of about $P = 500 \text{ mW/cm}^2$. All experiments were performed with an exposure time of 30 s. After irradiation, the photo-induced matter displacement was measured using an AFM working in tapping mode with silicon tips (PPP-NCHR from Nanosensors). The scan rate was 0.5 Hz.

Acknowledgement

TA and AH acknowledge financial support from the Région Grand Est and the European Union's FEDER fund. Samples were fabricated in the Nanomat platform (www.nanomat.eu). We acknowledge support from the French Agence Nationale de la Recherche (ANR) under grants 2D-CHIRAL (ANR-17-CE24-0039) and QUENOT (ANR-20-CE30-0033). This work has been done within the framework of the Graduate School NANO-PHOT (École Universitaire de Recherche, grant ANR-18-EURE-0013). This work was also partially supported by the HPC Center of Champagne-Ardenne ROMEO.

References

- (1) Wagnière, G. H. *On chirality and the universal asymmetry: reflections on image and mirror image*; John Wiley & Sons, 2007.

- (2) Collins, J. T.; Kuppe, C.; Hooper, D. C.; Sibilía, C.; Centini, M.; Valev, V. K. Chirality and Chiroptical Effects in Metal Nanostructures: Fundamentals and Current Trends. *Adv. Opt. Mat.* **2017**, *5*, 1700182.
- (3) Barron, L. D. *Molecular light scattering and optical activity*; Cambridge University Press, 2009.
- (4) Du, W.; Wen, X.; Gérard, D.; Qiu, C.-W.; Xiong, Q. Chiral plasmonics and enhanced chiral light-matter interactions. *Sci. China Phys. Mech. Astron.* **2020**, *63*, 1–11.
- (5) Goerlitzer, E. S. A.; Puri, A. S.; Moses, J. J.; Poulikakos, L. V.; Vogel, N. The Beginner’s Guide to Chiral Plasmonics: Mostly Harmless Theory and the Design of Large-Area Substrates. *Adv. Opt. Mat.* **2021**, *9*, 2100378.
- (6) Gansel, J. K.; Thiel, M.; Rill, M. S.; Decker, M.; Bade, K.; Saile, V.; von Freymann, G.; Linden, S.; Wegener, M. Gold helix photonic metamaterial as broadband circular polarizer. *Science* **2009**, *325*, 1513–1515.
- (7) Chen, Y.; Gao, J.; Yang, X. Direction-Controlled Bifunctional Metasurface Polarizers. *Laser Photonics Rev.* **2018**, *12*, 1800198.
- (8) Konishi, K.; Nomura, M.; Kumagai, N.; Iwamoto, S.; Arakawa, Y.; Kuwata-Gonokami, M. Circularly polarized light emission from semiconductor planar chiral nanostructures. *Phys. Rev. Lett.* **2011**, *106*, 057402.
- (9) Valev, V. K.; Baumberg, J. J.; De Clercq, B.; Braz, N.; Zheng, X.; Osley, E. J.; Vandendriessche, S.; Hojeij, M.; Blejean, C.; Mertens, J. et al. Nonlinear superchiral metasurfaces: Tuning chirality and disentangling non-reciprocity at the nanoscale. *Adv. Mater.* **2014**, *26*, 4074–4081.
- (10) Chen, Y.; Du, W.; Zhang, Q.; Ávalos-Ovando, O.; Wu, J.; Xu, Q.-H.; Liu, N.;

- Okamoto, H.; Govorov, A. O.; Xiong, Q. et al. Multidimensional nanoscopic chiroptics. *Nat. Rev. Phys.* **2022**, *4*, 113–124.
- (11) Tang, Y.; Cohen, A. E. Optical Chirality and Its Interaction with Matter. *Phys. Rev. Lett.* **2010**, *104*, 163901.
- (12) Hendry, E.; Carpy, T.; Johnston, J.; Popland, M.; Mikhaylovskiy, R. V.; Laphorn, A. J.; Kelly, S. M.; Barron, L. D.; Gadegaard, N.; Kadodwala, M. Ultra-sensitive detection and characterization of biomolecules using superchiral fields. *Nat. Nanotechnol.* **2010**, *5*, 783–787.
- (13) Tang, Y.; Cohen, A. E. Enhanced enantioselectivity in excitation of chiral molecules by superchiral light. *Science* **2011**, *332*, 333–336.
- (14) He, C.; Yang, G.; Kuai, Y.; Shan, S.; Yang, L.; Hu, J.; Zhang, D.; Zhang, Q.; Zou, G. Dissymmetry enhancement in enantioselective synthesis of helical polydiacetylene by application of superchiral light. *Nat. Commun.* **2018**, *9*, 1–8.
- (15) Negrín-Montecelo, Y.; Movsesyan, A.; Gao, J.; Burger, S.; Wang, Z. M.; Nlate, S.; Pouget, E.; Oda, R.; Comesaña-Hermo, M.; Govorov, A. O. et al. Chiral generation of hot carriers for polarization-sensitive plasmonic photocatalysis. *J. Am. Chem. Soc.* **2022**, *144*, 1663–1671.
- (16) Zu, S.; Han, T.; Jiang, M.; Lin, F.; Zhu, X.; Fang, Z. Deep-subwavelength resolving and manipulating of hidden chirality in achiral nanostructures. *ACS Nano* **2018**, *12*, 3908–3916.
- (17) Horrer, A.; Zhang, Y.; Gérard, D.; Béal, J.; Kociak, M.; Plain, J.; Bachelot, R. Local optical chirality induced by near-field mode interference in achiral plasmonic metamolecules. *Nano Lett.* **2019**, *20*, 509–516.

- (18) Narushima, T.; Okamoto, H. Strong nanoscale optical activity localized in two-dimensional chiral metal nanostructures. *J. Phys. Chem. C* **2013**, *117*, 23964–23969.
- (19) Hashiyada, S.; Narushima, T.; Okamoto, H. Local optical activity in achiral two-dimensional gold nanostructures. *J. Phys. Chem. C* **2014**, *118*, 22229–22233.
- (20) Valev, V. K.; Silhanek, A. V.; De Clercq, B.; Gillijns, W.; Jeyaram, Y.; Zheng, X.; Volskiy, V.; Aktsipetrov, O. A.; Vandenbosch, G. A. E.; Ameloot, M. et al. U-Shaped Switches for Optical Information Processing at the Nanoscale. *Small* **2011**, *7*, 2573–2576.
- (21) Zhou, S.; Li, J.; Lu, J.; Liu, H.; Kim, J.-Y.; Kim, A.; Yao, L.; Liu, C.; Qian, C.; Hood, Z. D. et al. Chiral assemblies of pinwheel superlattices on substrates. *Nature* **2022**, *612*, 259–265.
- (22) Plain, J.; Wiederrecht, G. P.; Gray, S. K.; Royer, P.; Bachelot, R. Multiscale optical imaging of complex fields based on the use of azobenzene nanomotors. *J. Phys. Chem. Lett.* **2013**, *4*, 2124–2132.
- (23) Hubert, C.; Bachelot, R.; Plain, J.; Kostcheev, S.; Lerondel, G.; Juan, M.; Royer, P.; Zou, S.; Schatz, G. C.; Wiederrecht, G. P. et al. Near-field polarization effects in molecular-motion-induced photochemical imaging. *J. Phys. Chem. C* **2008**, *112*, 4111–4116.
- (24) Haggui, M.; Dridi, M.; Plain, J.; Marguet, S.; Perez, H.; Schatz, G. C.; Wiederrecht, G. P.; Gray, S. K.; Bachelot, R. Spatial confinement of electromagnetic hot and cold spots in gold nanocubes. *ACS Nano* **2012**, *6*, 1299–1307.
- (25) Zhang, Y.; Demesy, G.; Haggui, M.; Gérard, D.; Béal, J.; Dodson, S.; Xiong, Q.; Plain, J.; Bonod, N.; Bachelot, R. Nanoscale switching of near-infrared hot spots in plasmonic oligomers probed by two-photon absorption in photopolymers. *ACS Photon.* **2017**, *5*, 918–928.

- (26) Gilbert, Y.; Bachelot, R.; Royer, P.; Bouhelier, A.; Wiederrecht, G. P.; Novotny, L. Longitudinal anisotropy of the photoinduced molecular migration in azobenzene polymer films. *Opt. Lett.* **2006**, *31*, 613–615.
- (27) Meinzer, N.; Hendry, E.; Barnes, W. L. Probing the chiral nature of electromagnetic fields surrounding plasmonic nanostructures. *Phys. Rev. B* **2013**, *88*, 041407.
- (28) Hendry, E.; Mikhaylovskiy, R.; Barron, L.; Kadodwala, M.; Davis, T. Chiral electromagnetic fields generated by arrays of nanoslits. *Nano Lett.* **2012**, *12*, 3640–3644.
- (29) Pachidis, P.; Cote, B. M.; Ferry, V. E. Tuning the polarization and directionality of photoluminescence of achiral quantum dot films with chiral nanorod dimer arrays: implications for luminescent applications. *ACS Appl. Nano Mater.* **2019**, *2*, 5681–5687.
- (30) Gilat, G. Chiral coefficient - a measure of the amount of structural chirality. *J. Phys. A: Math. Gen.* **1989**, *22*, L545.
- (31) Oshikiri, T.; Sun, Q.; Yamada, H.; Zu, S.; Sasaki, K.; Misawa, H. Extrinsic Chirality by Interference between Two Plasmonic Modes on an Achiral Rectangular Nanostructure. *ACS Nano* **2021**, *15*, 16802–16810.
- (32) Yan, C.; Wang, X.; Raziman, T.; Martin, O. J. Twisting fluorescence through extrinsic chiral antennas. *Nano Lett.* **2017**, *17*, 2265–2272.
- (33) Vinçon, I.; Wendisch, F. J.; De Gregorio, D.; Pritzl, S. D.; Akkerman, Q. A.; Ren, H.; de S. Menezes, L.; Maier, S. A.; Feldmann, J. Strong Polarization Dependent Nonlinear Excitation of a Perovskite Nanocrystal Monolayer on a Chiral Dielectric Nanoantenna Array. *ACS Photon.* **2022**, *9*, 3506–3514.